Nearly free surface silanols are the critical molecular moieties that initiate the toxicity of silica particles

Cristina Pavan[a,b,c], Rosangela Santalucia[b,d], Riccardo Leinardi[a,b,c], Marco Fabbiani[b,d], Yousof Yakoub[a], Francine Uwambayinema[a], Piero Ugliengo[b,d], Maura Tomatis[b,c,d], Gianmario Martra[b,c,d,1], Francesco Turci[b,c,d,2], Dominique Lison[a,2], and Bice Fubini[b,c]

[a]Louvain Centre for Toxicology and Applied Pharmacology, UCLouvain, 1200 Brussels, Belgium; [b]Department of Chemistry, University of Turin, 10124 Turin, Italy; [c]"G. Scansetti" Interdepartmental Centre for Studies on Asbestos and Other Toxic Particulates, 10125 Turin, Italy; and [d]Nanostructured Interfaces and Surfaces Interdepartmental Centre, 10125 Turin, Italy

Edited by Nils Kröger, Technische Universität Dresden, Dresden, Germany, and accepted by Editorial Board Member Lia Addadi September 2, 2020 (received for review May 4, 2020)

Inhalation of silica particles can induce inflammatory lung reactions that lead to silicosis and/or lung cancer when the particles are biopersistent. This toxic activity of silica dusts is extremely variable depending on their source and preparation methods. The exact molecular moiety that explains and predicts this variable toxicity of silica remains elusive. Here, we have identified a unique subfamily of silanols as the major determinant of silica particle toxicity. This population of "nearly free silanols" (NFS) appears on the surface of quartz particles upon fracture and can be modulated by thermal treatments. Density functional theory calculations indicates that NFS locate at an intersilanol distance of 4.00 to 6.00 Å and form weak mutual interactions. Thus, NFS could act as an energetically favorable moiety at the surface of silica for establishing interactions with cell membrane components to initiate toxicity. With ad hoc prepared model quartz particles enriched or depleted in NFS, we demonstrate that NFS drive toxicity, including membranolysis, in vitro proinflammatory activity, and lung inflammation. The toxic activity of NFS is confirmed with pyrogenic and vitreous amorphous silica particles, and industrial quartz samples with noncontrolled surfaces. Our results identify the missing key molecular moieties of the silica surface that initiate interactions with cell membranes, leading to pathological outcomes. NFS may explain other important interfacial processes involving silica particles.

silica | silanol | membrane | inflammation | quartz toxicity

Interfacial chemistry and molecular recognition patterns regulate the cross talk between endogenous organized materials and biomolecules or cells, e.g., in animal shells, bone, or dental tissues. These interactions are driven and finely tuned by the presentation of specific chemical and structural motifs on the surface of the material (1, 2), sometimes in synergy with their adsorbate (3). Similar phenomena regulate the interactions between biological environments and exogenous solids such as medical implants (4), vaccine adjuvants (5), nanomaterials (6, 7), or inhaled particles (8). Understanding the molecular determinant(s) at the heart of these interactions is critical for predicting and controlling expected and/or adverse outcomes of these foreign bodies.

Herein, we focus on the surface chemistry of silica particles. Silica is ubiquitous in the Earth's crust and universally used, both in crystalline and amorphous forms, mostly for its surface properties. Silicas are used in industrial productions and processes, including ceramics, glass, paints, plastics, construction products, catalysis, nanofabrication, and biomedical applications, in which the surface assumes a fundamental role (9–12). Some of us have recently shown that specific surface moieties of amorphous silica can catalyze amide bond formation, which has implications for prebiotic chemistry and the origin of life from silica minerals (13).

Crystalline silica is the leading cause of occupational respiratory disease worldwide (14). Millions of workers are exposed to respirable crystalline silica dusts, especially from new sources of exposure or because of the lack of attention for preventive management strategies (15). Excessive exposure to respirable crystalline silica dust generated by mining or grinding is associated with a spectrum of adverse health effects, including silicosis, autoimmune diseases, chronic obstructive pulmonary diseases, and lung cancer (16, 17). The Global Burden of Disease Study estimated that, in 2017, silicosis caused more than 10,000 deaths and over 200,000 y of life lost (18). Crystalline silica in the form of quartz or cristobalite is classified by the International Agency for Research on Cancer (IARC) as a human lung carcinogen (group 1) (19, 20). The toxicity of crystalline silica dust results from a sequence of mechanistic events, including membranolysis, activation of the NACHT, LRR, and PYD domains-containing protein 3 (NALP3) inflammasome complex, and proinflammatory cytokine production, which triggers lung inflammation and genotoxicity (21–24).

Amorphous silica is generally considered less toxic than crystalline silica, although available datasets are more limited (15, 25). While crystalline silica particles can cause persistent inflammation, leading to silicosis and/or lung cancer, amorphous silicas generally induce transient inflammatory responses (25–28). Amorphous

Significance

Silica particles with a population of nearly free silanols damage cellular membranes and initiate inflammatory reactions. Nearly free silanols are found on the surface of both fractured quartz and amorphous silica particles, and their occurrence initiates the toxicity of silica, thus revisiting the ancient paradigm whereby crystallinity is critical for silica toxicity. This finding resolves the lingering questions about the origin and the variability of the toxicity of silica particles. The discovery of the biological activity of nearly free silanols opens perspectives for the prevention of silicosis through a safer-by-design approach, and will have an impact on other fields that involve interfacial phenomena, including biomaterial design, nanofabrication, and catalysis.

Author contributions: C.P., D.L., and B.F. conceived the project; C.P., G.M., F.T., D.L., and B.F. designed research; C.P., R.S., R.L., M.F., Y.Y., F.U., P.U., and M.T. performed research; C.P., R.S., R.L., M.F., Y.Y., F.U., P.U., M.T., G.M., and F.T. analyzed data; and C.P., P.U., G.M., F.T., D.L., and B.F. wrote the paper.

Competing interest statement: The study was supported financially by the European Association of Industrial Silica Producers.

This article is a PNAS Direct Submission. N.K. is a guest editor invited by the Editorial Board.

See online for related content such as Commentaries.

[1]Deceased September 29, 2020.

[2]To whom correspondence may be addressed. Email: francesco.turci@unito.it or dominique.lison@uclouvain.be.

This article contains supporting information online at https://www.pnas.org/lookup/suppl/doi:10.1073/pnas.2008006117/-/DCSupplemental.

First published October 23, 2020.

silica does not appear to cause occupational lung disorders and is not classifiable as to its carcinogenic activity to humans (IARC group 3) (20). Thus, the paradigm of silica toxicity has generally considered crystallinity as a key hazardous property for silica particles. However, the toxic activity of silica particles varies widely depending on their source and preparation methods (26, 29–31), and several exceptions contradict the critical role of crystallinity for silica toxicity (24–26, 29–34). An example is given by pyrogenic amorphous silica that, contrary to other types of amorphous silica (e.g., Stöber silica, a colloidal silica), can induce lung inflammation (30) and increase collagen deposition after repeated dose administration in mice (35). Other studies showed that some Stöber silicas can cause inflammation in rodents (36, 37), and it is possible to vary the toxicity of pyrogenic silica by adjusting the synthesis conditions (31). The identification of the origin of this variability would represent a significant advance for developing rational production and use of safer silica materials.

Despite extensive research efforts in the past 50 y, the unifying factor that explains and predicts the toxicity of silica remains elusive. Of the variable features of silica particles, including size, morphology, polymorphism, and porosity, the surface state has been proposed as a significant component of the toxicity of silica particles (26, 29). Surface-promoted radical chemistry and surface-associated contaminants have been abundantly investigated in this context but did not fully match with the inflammatory activity of silica particles (ref. 38, and references therein). We considered, therefore, that the variable toxic activity of silica may be related to the heterogeneity of its surface chemistry, which involves siloxane bridges (≡Si–O–Si≡) and silanols [≡Si–OH, =Si(OH)$_2$] (38). Crystalline silica particles are generally obtained by mining or grinding, which upsets the long-range ordering of their crystal lattice and imparts surface disorder (39), similar to heterogeneous amorphous surfaces (10, 40). Silanols, which are generally more chemically reactive than siloxanes, can form variable patterns of mutual interactions, which depend on their structural (dis)organization and intersilanol distance (41).

Early studies proposed a role for silanols in the toxicity of silica (42, 43), but this hypothesis was not explored further. Recently, we proposed that silanols damage the phagolysosome membranes of lung macrophages, activating the NALP3 inflammasome and, in turn, leading to the release of the proinflammatory cytokine interleukin 1β (IL-1β) (44). However, this toxic activity of silica particles did not appear simply related to the overall silanol density (31, 45). Therefore, we hypothesized that, rather than silanols as a group, a specific surface silanol pattern might damage cell membranes and induce toxic responses (29). This idea was supported by the finding that the disorganization in the long-range spatial order of silanols induced by mechanical comminution of quartz crystals elicits membrane-damaging properties (34). This specific silanol pattern would be present on the surface of both amorphous and crystalline silicas and could thus represent a common molecular determinant of the toxicity of silica particles.

In the present work, we have newly identified a unique subfamily of silanols as major molecular determinants of the toxicity of silica particles. We synthesized, prepared, or collected model quartz and amorphous silica particles, and we tailored their surface silanol pattern through mechanical grinding or thermal treatments, simulating natural or industrially relevant processes. Surface specific analyses in highly controlled conditions were carried out by infrared (IR) spectroscopy to monitor the surface silanol populations before and after treatments, together with complementary physicochemical techniques to fully characterize the particles. The results show that "nearly free silanols" (NFS) promote membranolysis as assessed on model membranes, induce the release of the inflammatory cytokine IL-1β from macrophages, and initiate lung inflammation in a rat model. We applied a density functional theory (DFT) calculation to specifically define NFS based on their intersilanol distance, which affects their mutual chemical interactions, and, in turn, their availability for interacting with biomolecules and cell membrane components. This finding indicates that NFS, generated by fracturing α-quartz particles or originally present on different sources of amorphous silica, are the critical moieties for the molecular events that initiate the inflammatory responses to silica particles.

Results and Discussion

To uncover which surface silanol pattern is implicated in the toxicity of silica particles, we applied hydrothermal synthesis (46) to grow extremely pure α-quartz crystals in respirable size (gQ; "g": as-grown). These crystals displayed regular surfaces, at the nanometric resolution of field emission scanning electron microscopy (FE-SEM), and a hexagonal bipyramidal habit, typical of well-terminated quartz crystals (Fig. 1*A*). Fracturing this quartz mechanically (gQ-f; "f": fractured) mimicked the industrial processes used to produce or generate crystalline silica dusts from rocks, and induced the appearance of irregular planes of fracture (Fig. 1*B*). We assessed the toxic activity of these samples by measuring their membranolytic activity on red blood cells (RBCs), a predictor of the inflammatory activity of inhaled particles (44, 47). The membranolytic activity of gQ was as low as that of the negative reference particle, tungsten carbide (WC) (Fig. 1*C*). In contrast, gQ-f was almost as active as two quartz dusts of mineral origin obtained by fracturing, i.e., the commercial reference quartz (Min-U-Sil 5), which has well-documented pathogenic activity (19), and a highly pure laboratory-prepared quartz (mQ-f; "m": mineral). These results suggested that quartz fracturing introduces a specific surface state that causes cell membrane damage. Extensive physicochemical investigations (*SI Appendix*, Fig. S1 and Table S1) indicated that the high membranolytic activity of gQ-f, mQ-f, and Min-U-Sil 5, compared to pristine gQ, could not be ascribed to metal contaminants, particle size distribution, the potency to produce free radicals, or surface charge.

We used IR spectroscopy to inspect the surface silanols of these quartz samples after hydrogen–deuterium (H/D) exchange. Thus, the O-D stretching vibration (νOD) was measured under highly controlled conditions (Fig. 1*D* and *SI Appendix*, Fig. S2 *A* and *B*; see *SI Appendix*, *Supplementary Methods* for more details). The νOD silanol profile of gQ was dominated by a broad band (2,720 to 2,250 cm^{-1}) assigned to silanols mutually engaged in strong hydrogen bonds; this broad band resulted from the superimposition of subbands of hydrogen-bonded silanols on different types of α-quartz crystallographic surfaces (48) (Fig. 1*D*). After fracturing as-grown quartz crystals (gQ-f), the newly exposed surfaces appeared richer in silanols that experienced weak mutual interactions, evidenced by an increase in the intensity of the components at νOD > 2,720 cm^{-1}, particularly a component at 2,758 cm^{-1}. We defined this silanol population as NFS. Indeed, isolated, noninteracting silanols produced a different νOD signal at 2,762 cm^{-1} (i.e., the reference peak in Fig. 1*D*; see *SI Appendix*, Fig. S2*C* and *Supplementary Methods*). A DFT calculation of the νOD frequencies of two interacting silanol groups revealed that the signal attributed to NFS falls in the νOD range of silanols situated 4.00 to 6.00 Å apart on the silica surface (Fig. 2). Thus, the local arrangement of NFS definitely differs from proximate patches of silanols (2.5 to 2.8 Å apart) that mutually interact via strong hydrogen bonding (10) (Fig. 1*E*). This distinctive feature of NFS was also observed in the fractured mineral dusts Min-U-Sil 5 and mQ-f (Fig. 1*D*). Calculations based on the model developed by Carteret (49) (*SI Appendix*, *Supplementary Methods*) suggested that NFS, which contribute to the νOD signal at ∼2,758 cm^{-1}, represent about 3.5% of total silanols for gQ-f, 5.5% for Min-U-Sil 5 and mQ-f, and 1.0% for gQ.

To confirm that NFS determine the toxic activity of quartz particles, we performed thermal treatments to progressively tune surface silanol patterns of mQ-f (Fig. 3 *A*, *B*, and *B′*). After calcination at 450 °C, the overwhelming majority of mutually

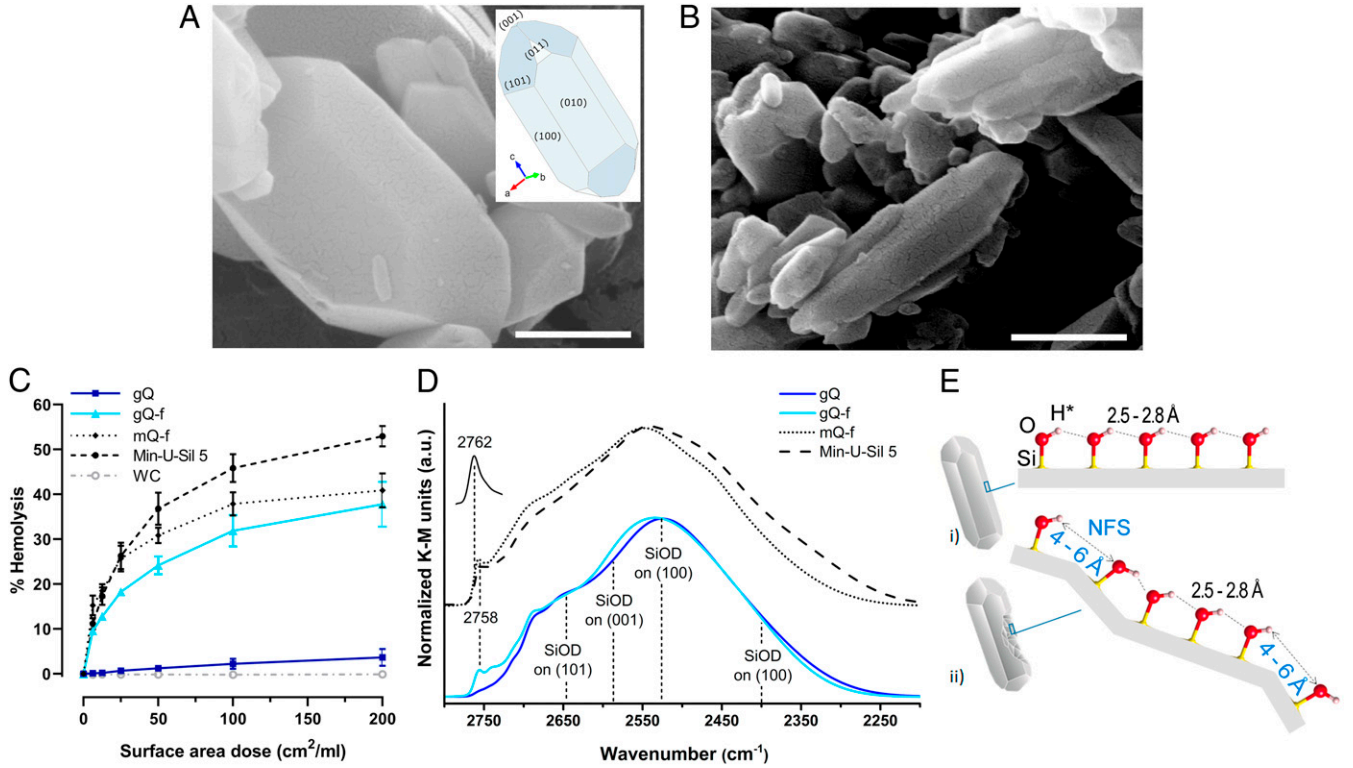

Fig. 1. Fracturing as-grown quartz crystals generates nearly free surface silanols that reproduce the membranolytic activity of mineral quartz dusts. (*A* and *B*) FE-SEM micrographs (scale bars, 400 nm) of (*A*) as-grown quartz crystals with regular surfaces (gQ) and (*B*) as-grown quartz crystals after fracturing by ball milling (gQ-f). *Inset* in *A* represents the hexagonal bipyramidal habit of a terminated quartz crystal with Miller (hkl) indices for crystal planes. (*C*) Membranolytic activity (percent hemolysis) of gQ compared to gQ-f, a pure quartz of mineral origin fractured by ball milling (mQ-f), Min-U-Sil 5 (positive reference quartz), and WC (negative reference particle). Data are mean ± SEM of three independent experiments. (*D*) Surface silanol distribution of quartz samples (after H/D exchange, reflectance IR spectra reported in Kubelka–Munk function). The reference peak at 2,762 cm^{-1} is assigned to isolated, noninteracting silanols, reported here to discriminate from the peak at 2,758 cm^{-1} assigned to weakly interacting, nearly free silanols (NFS). In the νOD region assigned to silanols mutually engaged in strong hydrogen bonds (2,720 to 2,250 cm^{-1}), SiOD on (*hkl*) refers to the assignment of the νOD subbands to hydrogen-bonded silanols on different types of α-quartz crystal surfaces (48). (*E*) Representation of the silanol patterns on as-grown quartz crystal surfaces (*i*) before and (*ii*) after fracturing: (*i*) regularly arranged, low distance, hydrogen bonded silanols, and (*ii*) disorganized, high distance, weakly interacting NFS, which interrupt the regularity of hydrogen bonded silanol chains. The values (in ångstroms) refer to the oxygen–oxygen distance between two silanols. The hydrogen (*) should be replaced with deuterium after H/D isotopic exchange.

hydrogen-bonded silanols (2,720 to 2,250 cm^{-1}) was irreversibly removed by condensation in siloxane bridges. Consequently, the silanol surface density declined (41) and the abundance of more distant NFS increased, as indicated by the up-shift, at 2,760 cm^{-1}, of the νOD component at the highest frequency (curves 1, 2, and 2–1 in Fig. 3 *A*, *B*, and *B′*). Calcination at 800 °C resulted in the removal of a significant proportion of the NFS detected at 2,758 cm^{-1} (curves 3 and 3–2 in Fig. 3 *A*, *B*, and *B′*), with a further shift of the peak toward isolated silanols (2,761 cm^{-1}). We compared these variations in surface silanol populations to the membranolytic activity of the pristine and calcined mQ-f samples (Fig. 3*C*). A strong decline in the abundance of hydrogen-bonded silanols, as well as an increase in the fraction of more distant NFS obtained by calcining at 450 °C, was accompanied by increased membranolytic activity. In contrast, the membranolytic activity drastically declined when the abundance of NFS declined after calcination at 800 °C. This finding supported the notion that NFS, whose abundance reached a maximum at intermediate levels of hydration, play a key role in the membranolytic activity of quartz particles.

To investigate whether the correlation between NFS and membranolytic activity only applies to crystalline silica forms, we examined the RBC membranolytic activity of an amorphous silica produced by pyrolysis (pS) ("p," pyrogenic; "S," silica). This silica sample, largely studied in surface chemistry (45, 50), has physicochemical characteristics completely different from those of quartz particles, including smaller size (primary particles, 10 to 120 nm), and a higher specific surface area (SSA) (~50 m^2/g) (50). We also calcined pS at an intermediate (450 °C) or high (700 °C) temperature to achieve the selective, irreversible removal of, first (at 450 °C), almost all hydrogen-bonded silanols, and then (at 700 °C) of NFS silanols that were ~5.5 Å apart (13) and characterized by the νOH band at 3,742 cm^{-1} (Fig. 3 *D* and *E*). The thermal treatments did not significantly modify the SSA of pS (13). The impact of these silanol changes on membranolytic activity (Fig. 3*F*) mirrored the observations with the pristine and calcined mQ-f samples. The removal of almost all hydrogen-bonded silanols caused a slight increase in membranolytic activity, whereas a decline in NFS resulted in a significant decline in membranolytic activity. In addition to reducing the NFS band, calcination of pS at 700 °C increased the formation of isolated silanols (νOH signal at 3,747 cm^{-1}). As the membranolytic activity of this calcined sample was reduced compared to the pristine or pS 450 °C samples, this indicates that isolated silanols are much less membranolytic than NFS species. Similar observations were reported in the past, when highly dehydroxylated surfaces bearing only isolated silanols displayed low membranolytic, cytotoxic, and inflammatory activity (45, 51–53). The average surface silanol density of the pS was far lower [i.e., ~1.5 OH/nm^2 (50)] than the average density expected

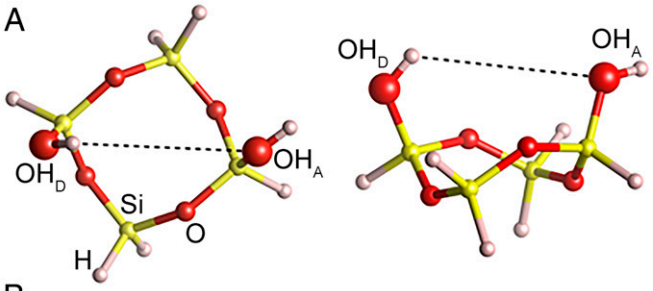

B

O···O (Å)	νOH$_D$ (cm^{-1})	νOH$_A$ (cm^{-1})	νOD$_D$ (cm^{-1})	νOD$_A$ (cm^{-1})
4.00	3708	3741	2735	2757
5.00	3734	3744	2752	2760
5.50	3739	3745	2756	2761
6.00	3743	3746	2760	2762

Fig. 2. Modeling of silanols interaction. (*A*) Top view (*Left*) and lateral view (*Right*) of a silica ring sporting two silanol groups in mutual hydrogen bond interaction. OH$_D$ and OH$_A$ stand for hydrogen bond donor or acceptor. (*B*) Oxygen/oxygen distances (Å) between two silanol groups, and OH or OD harmonic frequency (in centimeters^{-1}) of hydrogen/deuterium bond donor/acceptor. Harmonic νOH values were scaled by 0.959 with respect to the calculated DFT values (93), and νOD values were scaled with respect to νOH ones using factors reported by Chakarova et al. (94).

for α-quartz surfaces that reacted with water [i.e., a combination of ∼9.1 OD(OH)/nm^2 for {001} facets, 7.1 for {100} facets, and 5.6 for {011} facets (54)]. Hence, the contribution of NFS to membrane damage appeared to be independent of the intrinsic structure of the silica particles (based on crystallinity, size, and surface origin) and of overall silanol density.

Environmental silica dusts typically contain contaminants and generate free radicals, features that may contribute to the pathogenic activity of silica (20). We extended our studies to include a panel of industrial quartz dusts (iQ1-4) that were similar in size, SSA, and potency to generate free radicals, but that were less pure than the quartz dusts used above (*SI Appendix*, Fig. S3 *A–C*). We also included industrial vitreous silica (vS), an amorphous material with high SSA. This material differs from pyrogenic silica and, like pS (45), does not generate free radicals (*SI Appendix*, Fig. S3 *A–C*). The membranolytic activity of the industrial quartz dusts (iQ1-4) did not correlate with any physicochemical feature other than the intensity of the IR signal assigned to NFS related to the overall silanol pattern (*SI Appendix*, Fig. S3 *D* and *E*). The spectral components due to NFS dominated the high-frequency IR signal for vS, which had a strong membranolytic activity (*SI Appendix*, Fig. S3 *F* and *G*). This finding confirmed that crystallinity is not required for NFS formation or membranolytic activity.

We further established the relevance of NFS to the pathogenic activity of silica by using in vitro and in vivo models that addressed the subsequent biological events induced by membrane damage, and which sequentially lead to inflammation. Upon inhalation, quartz particles damage the phagolysosome membrane of alveolar macrophages. This early event triggers NALP3-dependent proinflammatory responses, such as the processing and release of the proinflammatory cytokine IL-1β (21–23). Based on the above results, we tested the panel of model quartz particles characterized by enriched or depleted NFS content (i.e., gQ vs. gQ-f or mQ-f vs. mQ-f calcined at 800 °C, respectively). These quartz samples did not differ in other physicochemical features (*SI Appendix*, Fig. S1 and Table S1), thus allowing the isolation of the contribution of NFS to the toxicological outcome. We evaluated the release of IL-1β from differentiated THP-1 human macrophages, induced by noncytotoxic doses of quartz particles enriched or depleted in NFS (Fig. 4 and *SI Appendix*, Fig. S4 *A* and *B*). The amplitude of IL-1β release reflected the quantitative variations in NFS. Thus, NFS could also damage phagolysosomes and induce NALP3-dependent proinflammatory responses.

We explored the lung inflammatory response to NFS-enriched or -depleted quartz samples in a rat bioassay. NFS-enriched quartz (gQ-f), but not intact quartz (gQ), induced the recruitment of a significant number of inflammatory cells (Fig. 5*A*), particularly neutrophils (Fig. 5 *B* and *C*), a strong cytotoxic effect (Fig. 5*D*), and increased alveolo-capillary permeability (Fig. 5*E*). Notably, gQ did not induce an inflammatory reaction or an increase in alveolo-capillary permeability, even at high doses (5 mg), and it only exerted a very modest cytotoxic effect (*SI Appendix*, Fig. S4 *C–F*). The mineral quartz dust (mQ-f) induced strong inflammatory and cytotoxic responses, which were markedly attenuated when the dust was depleted of NFS after thermal treatment (mQ-f 800 °C; Fig. 5 *A–E*). The Min-U-Sil 5 quartz, used here as a positive reference particle, exerted an inflammogenic activity, which, also for this sample, was related to the presence of surface NFS (Fig. 1*D*).

The carcinogenic activity of crystalline silica is related to its secondary genotoxic activity, mediated by persistent inflammation and neutrophil recruitment (55). Therefore, we investigated whether the presence of NFS might determine the genotoxic activity of crystalline silica in epithelial lung cells in vivo. Micronuclei were quantified in type II pneumocytes isolated from rat lungs 3 d after the administration of mQ-f or mQ-f 800 °C (Fig. 5*F*). The micronucleus frequencies were lower with mQ-f 800 °C than with mQ-f treatment, and notably higher with mQ-f than with vehicle treatment (Ctl). Overall, the lung inflammatory reactions to quartz particles appeared regulated by the quantitative variations in surface NFS.

At the molecular level, the interaction between silica and biological membranes in aqueous systems is mediated by silanol deprotonation equilibria, the presence of electrolytes, and biomacromolecules (56–59). Despite this great complexity, the toxic activity of NFS is consistent with the impact of intersilanol distance on the strength of their mutual bonds (48, 54, 60, 61). Computational studies have shown that the surface energy of silica is mostly determined by the properties of the hydrogen bonds formed at the silica surface. In general, the stronger the mutual hydrogen bond interactions, the lower the surface interaction energy (54, 60). This phenomenon has been demonstrated at the interface between quartz and liquid water, where strong hydrogen bonds between surface silanols were preserved, and weak hydrogen bonds were easily broken by the surrounding water molecules (61). Thus, conceivably, the most active silica moiety for interacting with biomembranes is the one that requires the least energy to break established intersilanol bonds. NFS are mutually connected by weak interactions (e.g., weak hydrogen bonds, or van der Waals forces), which can favor external intermolecular interactions. As documented here and in previous investigations (45, 51–53), a heated (highly hydrophobic/dehydroxylated) silica surface displaying only a few isolated silanols does not appear to efficiently interact with membranes. The difference between surfaces characterized by NFS and others presenting only fully isolated silanols may reside in the quasi-vicinal nature of NFS compared to the fully free silanols (>6 Å apart). Fig. 6 shows a model of the interaction between a phosphatidylcholine molecule, chosen as a representative building block of biological membranes, and a NFS pair. The structure is derived from a geometry relaxation that occurs by minimizing the total energy at the GFN-FF level, a newly developed force field that gives the structure of intermolecular complexes and the corresponding interaction energies in excellent agreement with a high level of theory [DFT or even CCSD(T) for hydrogen bonds]. According to this model, the

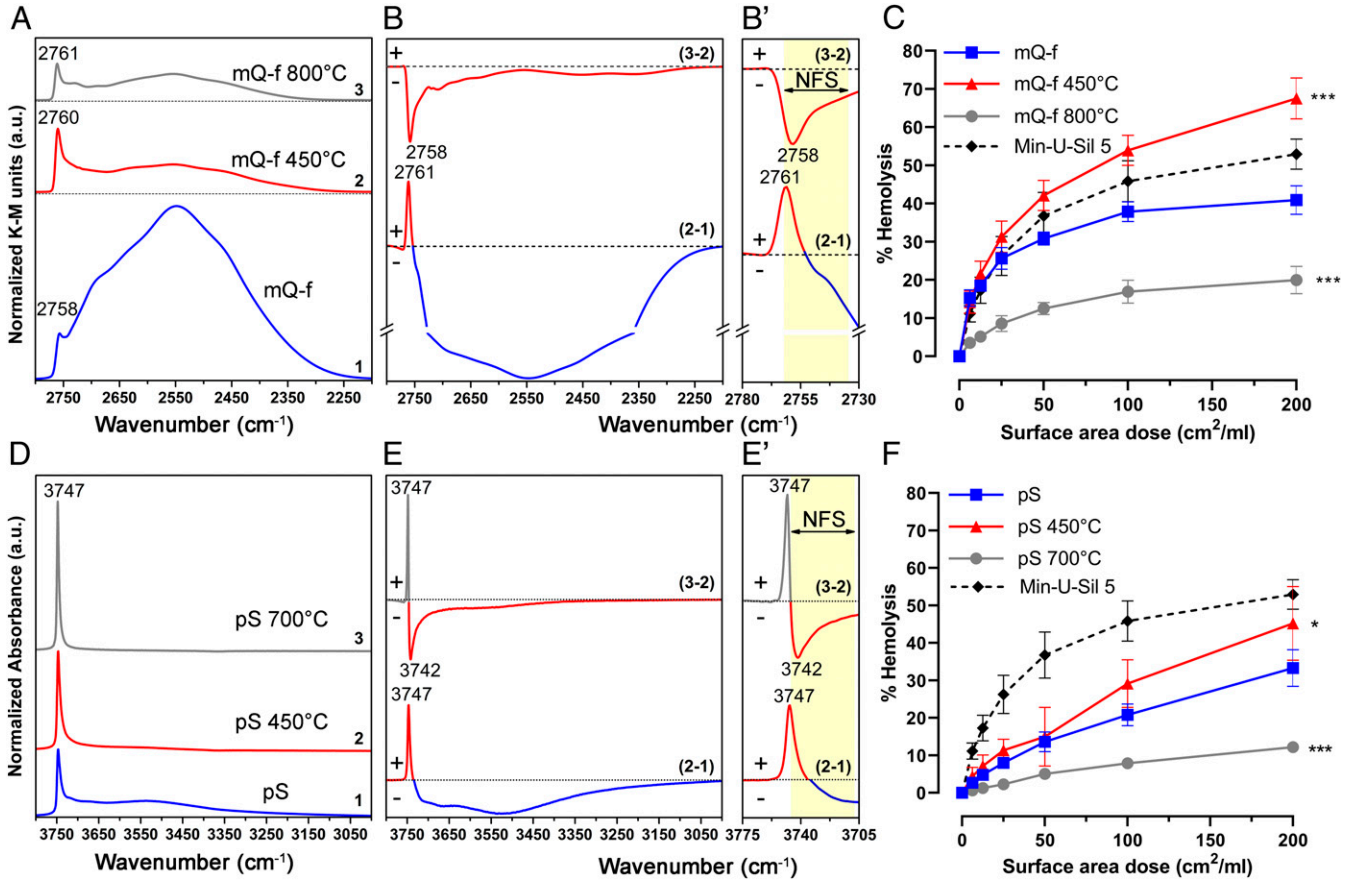

Fig. 3. Nearly-free silanols (NFS) determine the membranolytic activity of crystalline and amorphous silica particles. (*A*–*C*) Relative variation of NFS determines the membranolytic activity of fractured mineral quartz particles (mQ-f). (*A*) Surface silanol distribution (after H/D exchange, reflectance IR spectra reported in Kubelka–Munk function) of 1) pristine mQ-f (at room temperature [r.t.]), 2) mQ-f calcined at 450 °C, and 3) mQ-f calcined at 800 °C. (*B* and *B′*) Differences in silanol population (between pairs of spectra in *A*) as a result of thermal treatments: (2−1) calcined at 450 °C – pristine, (3−2) calcined at 800 °C – calcined at 450 °C. (*B′*) Enlarged section of the difference spectra (*B*) showing the νOD spectral region of NFS (2,762 to 2,735 cm^{-1}) and isolated silanols. (*C*) Membranolytic activity (percent hemolysis) of pristine and calcined mQ-f samples, and Min-U-Sil 5 (positive reference particle). (*D*–*F*) NFS are present on amorphous pyrogenic silica (pS) and determine its membranolytic activity. (*D*) Surface silanol distribution (transmittance IR spectra reported in absorbance) of (1) pristine pS, (2) pS calcined at 450 °C, and (3) pS calcined at 700 °C. (*E* and *E′*) Differences in silanol population (between pairs of spectra in *D*) as a result of thermal treatments: (2−1) calcined at 450 °C – pristine; (3−2) calcined at 700 °C – calcined at 450 °C. (*E′*) Enlarged section of the difference spectra (*E*) showing the νOH spectral region of NFS (3,746 to 3,708 cm^{-1}) and isolated silanols. Panels *D* and *E* are adapted from Rimola et al. (13). (*F*) Membranolytic activity (percent hemolysis) of pristine and calcined pS samples, and Min-U-Sil 5 (positive reference particle). Data in *C* and *F* are mean ± SEM of three independent experiments; *P* values of calcined samples compared to the pristine ones determined by two-way ANOVA followed by Dunnett's post hoc test (mean effect): $*P = 0.0206$; $***P < 0.001$.

resulting binding energy of 125 kJ/mol may allow clamping rather strongly the negatively charged phosphate group of the phospholipid head between the two NFS. The same type of interaction could not occur with isolated silanols that can only make one single interaction, almost half as strong as that for the NFS pair. The clamping of the NFS may stiffen the membrane, making it more prone to breaking due to these coupling points, which would impair its natural flexibility.

Our study is limited by the low relative amount of NFS and the very low SSA of quartz samples, which do not currently allow us to address additional aspects experimentally, including macroscopic observables, such as pK, wettability, and surface hydration. Also, the model in Fig. 6 deals with NFS and a phospholipid in direct contact, assumed to be a plausible scenario. As surface chemical heterogeneity modulates the silica surface hydration (40), it would be interesting to investigate whether NFS plays a role in this interfacial hydration layer, and its relevance for the interactions with membranes.

Two main categories of surface functionalities have been proposed in the past to account for silica toxicity, namely silanols and reactive oxygen species (ROS)-generating sites, which fitted a relatively limited set of samples, but both failed to apply when larger numbers of silica sources were examined. Our NFS model does not contradict most of these hypotheses but explains some apparent inconsistencies. Most of previous investigations considered only the total content of silanols, often finding discrepancies with membranolysis or cytotoxicity (31, 45). The present identification of the membranolytic activity of NFS may clarify why some dense polymorphs of crystalline silica, i.e., stishovite, were not active in toxicological studies (62). Indeed, previous IR investigations showed that the surface silanol patterns of stishovite differed from those in most silicas, as almost all silanols are involved in strong hydrogen-bonding interactions due to the peculiar crystallographic structure (octahedral coordination of Si atoms) of this polymorph (33). Our NFS model may also explain why colloidal silica (i.e., precipitated or Stöber silica), which is obtained in aqueous solution and usually displays a large density of strongly hydrogen-bonded silanols (50), often appears nonmembranolytic or noninflammatory (25, 26, 30, 63).

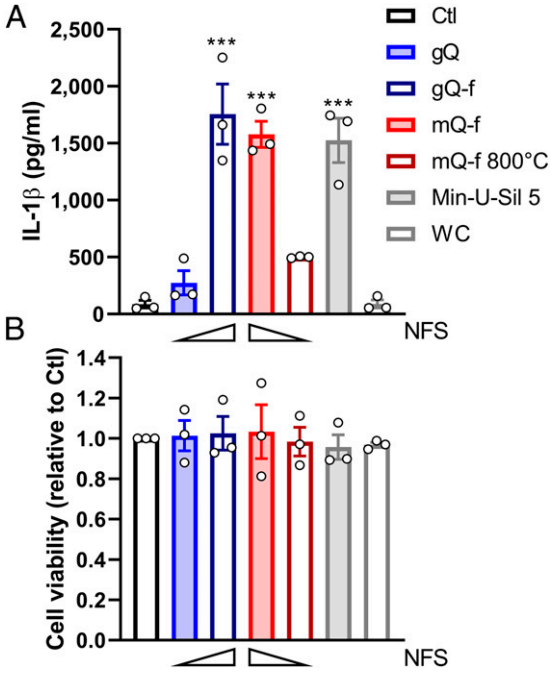

Fig. 4. Nearly-free silanols (NFS) determine the proinflammatory activity of quartz particles in vitro. (*A*) Release of IL-1β from and (*B*) cell viability of differentiated THP-1 macrophages 24 h after exposure to vehicle (Ctl) or quartz particles enriched or depleted in NFS, i.e., gQ, gQ-f (10 cm^2/mL), mQ-f, mQ-f 800 °C (5 cm^2/mL), Min-U-Sil 5 as positive reference quartz (5 cm^2/mL), and WC as negative reference particle (5 cm^2/mL). Wedges illustrate relative content of NFS. Data are mean ± SEM of three independent experiments. Each dot represents the average of four technical replicates for each independent experiment. For IL-1β values (*A*), one-way ANOVA with Dunnett's post hoc test was applied to compare treated groups vs. Ctl; ***$P < 0.001$. IL-1β values were also compared with a two-tailed Student's *t* test: gQ vs. gQ-f: $P = 0.007$; mQ-f vs. mQ-f 800 °C: $P < 0.001$. For cell viability (*B*), one-way ANOVA was n.s.

Other studies in the past, including some of our investigations, proposed a mechanism of silica toxicity based on particle-associated radicals (e.g., silyl, siloxyl radicals) and ROS (e.g., hydroxyl, superoxide, and peroxyl radicals), the latter originating from the reaction with atmospheric components of dangling bonds upon fracture/grinding of the particles (64, 65) or opening of strained three-membered siloxane rings (30). In some proinflammatory and profibrogenic cell-signaling pathways and transcription factor activation, the triggering role of particle ROS cannot be disregarded (66–69), and they can contribute to increasing the oxidative stress in the lung milieu (20). The present data clearly document that particle ROS are not critical for membrane damage initiated by silica particles, as also shown in previous studies (45, 70–72). Our pyrogenic and vitreous silicas do not generate hydroxyl radicals (pyrogenic silica data are reported in ref. 45), but are highly membranolytic. The highly membranolytic mQ-f does not generate free radicals either. Thus, for the mechanism of silica interaction with the cell membrane, our data indicate that particle-derived ROS are not immediately critical. The NFS model may offer an alternative hypothesis to explain the membranolytic activity of a fumed silica sample, which was associated with hydroxyl radicals originating from a population of strained three-membered siloxane rings (30). We demonstrate that NFS are present on the surface of a variety of silica materials; thus, NFS could also have been present on that specific fumed silica sample. Moreover, the role of strained three-membered siloxane rings was suggested to specifically apply to amorphous silica, not to quartz surface (30). In this sense, our work integrates previous models and offers a more general approach for both crystalline and amorphous silica.

Increasing evidence has shown at the RBC surface the presence of submicrometric lipid domains that contribute to plasma membrane tension regulation and deformation (73). Recently, nanoscale protrusions (from 50 to 500 nm in diameter and from 10 to 100 nm in height) of sphingomyelin-enriched lipid domains were observed at the RBC surface that regulate the stiffness of RBCs (74). These lipid domains, which impart differential mechanical properties, might also be involved in the interaction with particles. The same lipid microdomains, also called rafts, are found in endosomes/lysosomes, where they regulate trafficking in cells (75, 76). In agreement with our proposed model of interaction of NFS with membranes (Fig. 6), previous investigations (77, 78) related silica toxicity to its capacity to strongly coordinate via hydrogen bonding the phosphate groups of phospholipids, decreasing their mobility in phospholipid bilayers.

We may hypothesize that NFS interact with the membrane of the phagolysosomes, after phagocytosis by alveolar macrophages, similarly to the interaction established with the RBC membrane (79). Destabilization of the phagolysosome membrane leads to the release of the phagolysosome content, including cathepsins, into the cytosol of macrophages, triggering the activation of the NALP3 inflammasome (21). Inflammasome assembly is crucial for activating the proteolytic enzyme caspase-1, which initiates cell death and controls the maturation and secretion of IL-1β and IL-18. These proinflammatory and chemotactic cytokines induce neutrophil influx and account for the acute and chronic inflammatory response when persistently overproduced. While the upstream biochemical mechanism of NALP3 inflammasome activation may also involve ROS generation and intracellular Ca^{2+} (ref. 80, and references therein), several studies observed that both phagolysosome destabilization induced by particles (21, 44, 81) and pharmacological disruption of lysosomes (21) are sufficient to activate the NALP3 inflammasome, which is involved in both crystalline and amorphous silicas-induced inflammation (21–24, 81–83). However, we observed slight differences between membranolysis, in vitro inflammation, and in vivo inflammation trends that may be due to increased complexity and other cellular contributors such as, for instance, cell-derived ROS.

Notably, although being of completely different crystal structures, monosodium urate and fractured silica share the ability to form strong hydrogen bonds with membrane phospholipids, to activate the inflammasome, and to induce inflammatory reactions (84), thus suggesting a common mechanism of pattern recognition.

Conclusions

Our results reveal the critical role of a specific family of silanols, referred to here as NFS, and show that the local density of silanols, not their total amount or average density, determines the toxic activity of silica dusts. This finding applies to all silica samples investigated, irrespective of their crystalline or amorphous structure. Surface NFS emerge as the elusive element that reconciles the enigmatic inflammatory responses observed with both crystalline and amorphous silica in several experimental studies (24, 25, 32). Thus, this finding imposes a reconsideration of the paradigm according to which crystallinity is a key determinant of silica particle toxicity. The present data indicate that crystalline and amorphous silicas exist as a continuum of forms with variable toxic activity depending on their surface NFS content. The biopersistence of inhaled particles is another important determinant of their toxicity. While crystalline silica persists in the lung, amorphous silica particles are, in general, rapidly cleared through dissolution and macrophage removal (85–87). However, some less soluble amorphous samples that express surface NFS could be hazardous, such as vS, which is very reactive in vitro (88), or pyrogenic silica, which is inflammatory in vivo (53).

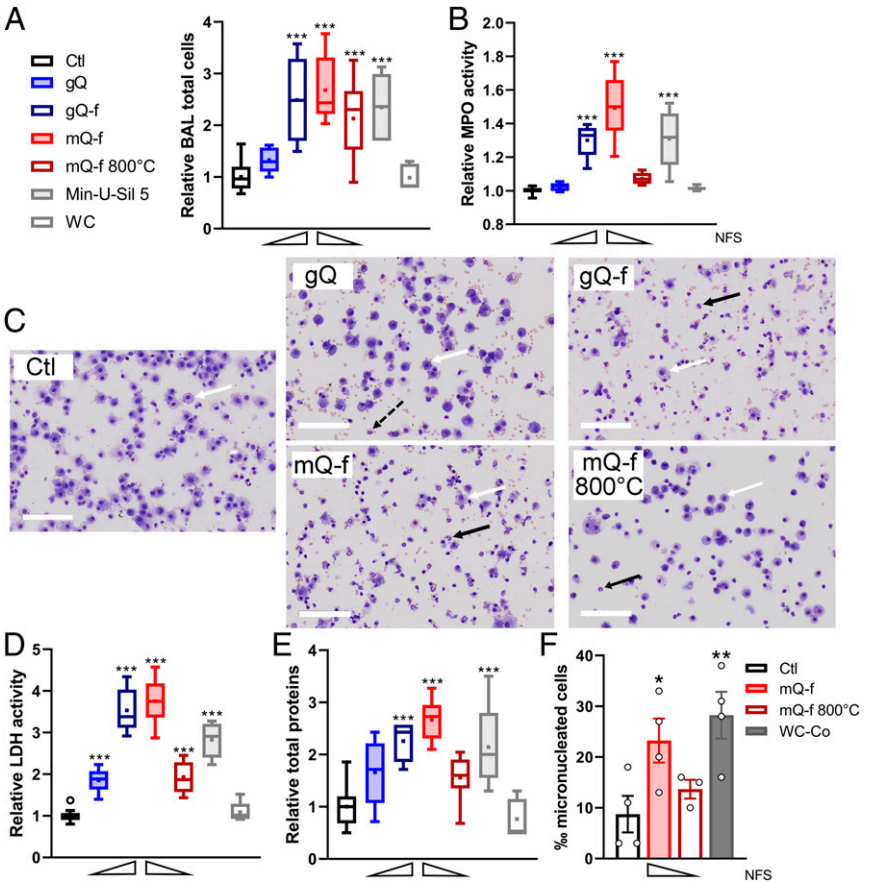

Fig. 5. Nearly-free silanols (NFS) determine the inflammatory response to quartz particles in vivo. (*A–E*) Inflammatory responses in the lung of rats 72 h after administration of vehicle (Ctl) or quartz particles enriched or depleted in NFS, i.e., gQ, gQ-f (2.5 mg, $n = 5$), mQ-f, mQ-f 800 °C (0.75 mg, $n = 9$), Min-U-Sil 5 as positive reference quartz (0.75 mg, $n = 5$), WC as negative reference particle (0.75 mg, $n = 5$). (*A*) Total cell count in bronchoalveolar lavage (BAL) (two-tailed Student's *t* test, gQ vs. gQ-f: $P = 0.017$; mQ-f vs. mQ-f 800 °C: $P = 0.121$), (*B*) BAL myeloperoxidase (MPO) activity (gQ vs. gQ-f: $P < 0.001$; mQ-f vs. mQ-f 800 °C: $P < 0.001$), (*C*) representative BAL cell populations (scale bars, 100 μm; white arrows indicate macrophages; black arrows indicate neutrophils; dotted black arrow indicates eosinophils), (*D*) BAL lactate dehydrogenase (LDH) activity (gQ vs. gQ-f: $P < 0.001$, mQ-f vs. mQ-f 800 °C: < 0.001), (*E*) BAL total protein concentration (gQ vs. gQ-f: $P = 0.111$, mQ-f vs. mQ-f 800 °C: $P < 0.001$). Data are presented as box plots (Tukey style; center line, median; square points, means; box limits, upper and lower quartiles; whiskers, 1.5 × IQR; empty circle, outliers) of relative values to Ctl ($n = 14$) set at 1. Wedges illustrate relative content of NFS. One-way ANOVA with Dunnett's post hoc test was applied to compare treated groups vs. Ctl; ***$P < 0.001$. (*F*) Mutagenic response as measured by micronucleus frequency in type II epithelial cells in rat lungs after administration of vehicle (Ctl), mQ-f, mQ-f 800 °C (0.75 mg), or WC-Co as a positive reference particle (2 mg). Dots are individual rats. Data are means ± SEM ($n = 3$ to 4 rats per group). One-way ANOVA with Dunnett's post hoc test was applied to compare treated groups vs. Ctl; *$P < 0.05$, **$P < 0.01$. Two-tailed Student's *t* test, mQ-f vs. mQ-f 800 °C: $P = 0.133$.

The identification of the pathogenic role of NFS clarifies the exact nature of the surface state that accounts for the variable pathogenic activity of crystalline silica (29). Importantly, we show here that a pure quartz, grown to a respirable size, does not induce lung inflammation. Fracturing, which is the only practical means of obtaining quartz dust in industrially significant amounts, is a critical step that increases the degree of surface disorder and introduces NFS, which are otherwise rare on terminated surfaces of as-grown quartz crystals.

Our discovery that the NFS population is a surface determinant of the toxicity of silica particles is relevant for the development of predictive toxicological testing. More generally, NFS might also contribute to molecular recognition mechanisms that orchestrate interactions between human immune responses and silica-based (bio)materials. The present findings can also inform biomedical and technological applications that involve adsorption processes on silica materials.

Materials and Methods

Particles.

Model quartz samples. As-grown quartz crystals (gQ) were obtained by hydrothermal synthesis following a procedure previously described (46), with minor modifications. Briefly, a 25% (wt/wt) sodium metasilicate pentahydrate aqueous solution was polymerized using mineral acids until gel formation. The gel was stabilized at pH ~8. Growth runs were performed in PFTE liner sealed into steel autoclaves at 210 °C and autogenic pressure for 168 h. Each lot deriving from each synthesis run was verified for crystallinity by X-ray diffraction (XRD) analysis. One gram of synthetic quartz was sieved in a double sieve with 100- and 30-μm meshes on a vibrating apparatus for 30 min. The fraction <30 μm was used as such (gQ); the fraction >30 μm was used to produce fractured as-grown quartz (gQ-f), with a similar size as gQ. For gQ-f, 500 mg of the fraction >30 μm was ground in a mixer mill (Retsch MM200) in agate jars, with two agate balls of 6 mm diameter per jar, at 27 Hz from 1 to 6 h. Differences in grinding time were due to differences in SSA and size of the pristine material, in order to achieve, at the end of the milling procedure, bulk characteristics similar to the reference quartz dust (Min-U-Si-5).

The mineral fractured quartz (mQ-f) was obtained by milling centimetric quartz crystals from Madagascar in a planetary ball mill (Retsch S100), in an agate jar with one agate ball (25 mm), for 3 h at 70 rpm. Then, 500 mg of the obtained dust was further milled in a mixer mill (Retsch MM200), in an agate jar with two agate balls of 6 mm, for 4 h at 27 Hz. This protocol was selected based on a systematic analysis of the particle size distribution at the end of intermediate milling times.

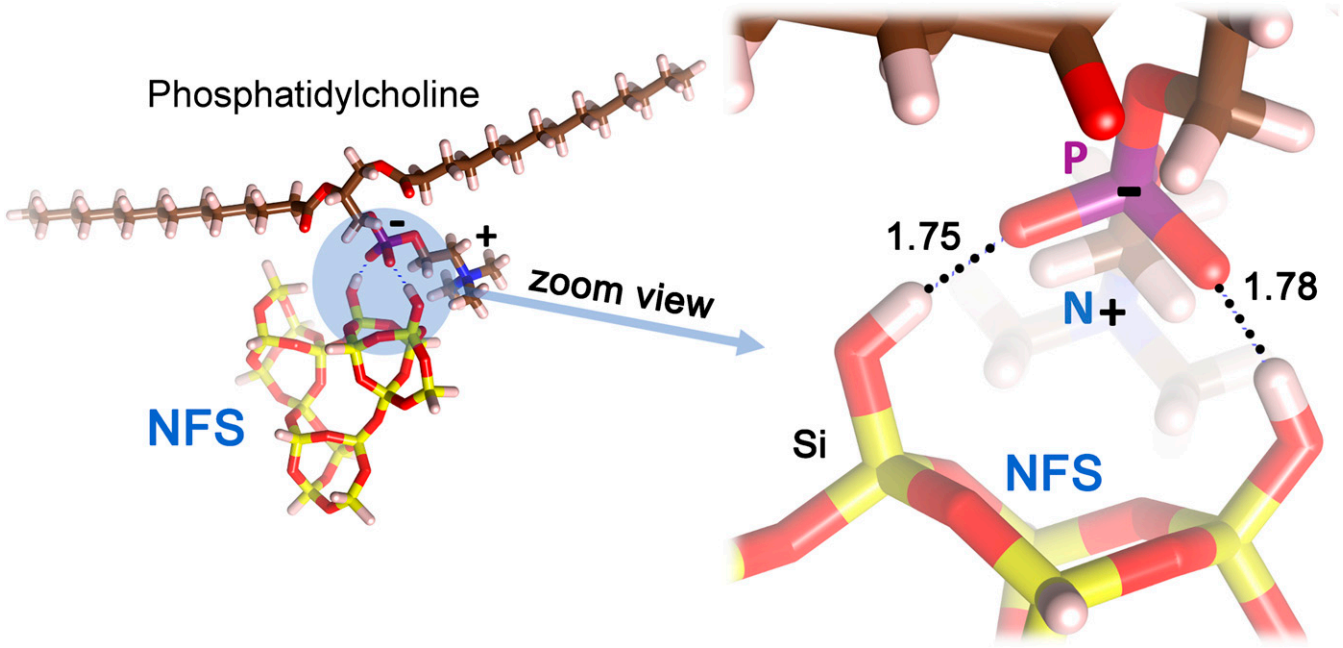

Fig. 6. A cluster model of nearly-free silanols (NFS) interacting with phosphatidylcholine, a building block of cell membranes, as predicted by the GFN-FF calculations. The H···O hydrogen bond distances between the NFS and the oxygens of the negatively charged phosphate group are in ångströms.

Industrial silica samples. Industrial mineral quartz dusts (iQ1-4) and a vS were obtained from industrial producers. A pyrogenic amorphous silica (pS; Aerosil OX50; Degussa) was also included.
Reference samples. The commercial quartz Min-U-Sil 5 (US Silica Company) was used as positive reference particle with well-documented toxic effects (19). Tungsten carbide (WC) or tungsten carbide-cobalt mixture dusts (WC-Co) were selected as negative or positive reference particles, respectively, depending on the toxicological endpoint assessed (89, 90).

Heat Treatments of the Particles. To obtain the mQ-f 450 °C or mQ-f 800 °C, 100 or 500 mg of mQ-f, respectively, were heated in a muffle furnace for 2 h at the indicated temperatures (ramp up: 10 °C/min) and allowed to cool at room temperature (r.t.) in the same furnace. To obtain pS 450 °C or pS 700 °C, 100 mg of the pristine powder was pressed into self-supporting pellets, then heated at 450 °C for 2.5 h, or in a two-step process, respectively: 1) the material was heated at 450 °C for 2.5 h, allowed to cool at r.t. and, 2) reheated at 700 °C for 7.5 h. The temperatures and modus operandi were selected based on previous studies on crystalline (45) and amorphous silica (13).

Particle Morphology. FE-SEM with an Inspect F microscope (FEI) was used. Dry quartz particles were deposited on conductive stubs and coated with gold to prevent the electron beam from charging the sample. The operating conditions were: HV 20 kV, WD 10–15 mm.

Crystallinity. XRD analysis (PW3040/60 X'Pert PRO MPD diffractometer, PANalytical) was used in capillary configuration. The source was a high-power ceramic tube PW3373/10 LFF with a Cu anode. Spectra were collected in the (5 to 90°) 2θ range, with 45 s as time per step, and Cu Kα radiation at 45 kV, and 40 mA. The diffractograms obtained were compared with the National Institute of Standards and Technology Standard Reference Material 1878b (Respirable Alpha Quartz) pattern.

SSA. SSA was measured by using the ASAP 2020 apparatus (Micromeritics), and data analyzed with the Brunauer, Emmet, and Teller (BET) method. Samples were first outgassed at 150 °C for 2 h. Depending on the SSA expected, Kr (SSA $\leq$ 5 m^2/g) or N_2 (SSA >5 m^2/g) adsorption at −196 °C was applied.

Size. Particle size distribution was measured using a flow particle image analyzer (FPIA-3000S; Malvern Instruments) by flowing 5 mL of particle suspension through a flat cell where images of the particles are captured using stroboscopic illumination and a charge-coupled device camera. Particle suspensions (1 mg/mL in water) were sonicated for 2 min (horn, 3 mm; frequency, 20 kHz; maximum power output, 25 W; amplitude, 120 μm) with an ultrasonic probe (Sonopuls HD 3100; Bandelin) before injection into the measurement cell, then stirred at 360 rpm to avoid particle sedimentation. Data were obtained from two or three independent measurements, three replicates for each measurement, and processed by the Sysmex FPIA software (version 00-13). The detection range was 0.8 to 160 μm. The average diameter expressed as circle equivalent (CE) diameter and the value of the CE diameter below which 90% of observations fall (D90) were reported.

Elemental Analysis. Transition metal traces were assessed by energy dispersive X-ray analysis with a scanning electron microscope (JEOL JSM IT300LV), and an Oxford INCA Energy 200 spectrometer with an INCA X-act SDD thin window detector.

Surface Charge. The surface charge was assessed as ς-potential by electrophoretic light scattering (Zetasizer Nano-ZS; Malvern Instruments). Silica particles were suspended in 0.01 M phosphate buffer solution (PBS) or 0.01 M NaCl (from 1 to 10 mg, in order to have attenuator ∼8, in 10 mL of solution) and sonicated for 2 min on ice with the ultrasonic probe. The pH of the suspension was measured after 5 min with a digital in situ calibrated pH meter (827 pH Lab; Metrohm). At least three independent measurements were performed for each sample, five runs for each measurement.

IR Spectroscopy. For quartz powders, constituted by particles large enough to heavily scatter IR light, IR measurements were carried out in the diffuse reflectance mode, using a Spectra-Tech diffuse reflectance unit, equipped with an environmental chamber allowing the connection to a conventional vacuum line (residual pressure, $\leq 1 \times 10^{-4}$ mbar), and to carry out in situ all desorption/adsorption experiments. The samples were analyzed in powder form, with ∼50 mg of silica sample. The spectra were collected with a Bruker IFS66 FTIR spectrometer (Globar source, MCT detector; resolution, 2 cm^{-1}) averaging 256 scans for spectrum to obtain a good signal-to-noise ratio. The background was recorded in air with finely ground, dry KBr as reference. As detailed in *SI Appendix*, the silica samples underwent an H/D isotopic exchange by adsorption/desorption of D_2O (Sigma-Aldrich; 99.90% D) in order to convert surface silanols (SiOH) in the SiOD form. For pS and vS samples, the smaller size of the particles and higher SSA compared to quartz dusts, allowed the collection of IR in the transmission mode. Aliquots of the two powdered samples were pressed in self-supporting pellets and placed in a quartz cell equipped with CaF_2 windows. Spectra were recorded with a Bruker IFS28 FTIR spectrometer (Globar source, DTGS detector; resolution, 2 cm^{-1}) by accumulating 150 coadded scans to attain a good signal-to-noise

ratio. The cell was attached to a conventional vacuum line (residual pressure, $\lesssim 1 \times 10^{-4}$ mbar) allowing adsorption–desorption experiments to be carried out in situ. In a specific experiment, a pellet of pS calcined at 700 °C underwent the H/D isotopic exchange, in order to determine experimentally the νSiO-D signal of isolated silanols.

Computational Details. All geometry optimization and vibrational frequencies were run at DFT level using the B3LYP-D3(BJ)/6-311++G(2d,2p) method (91) on a silica model envisaging a silica ring with two silanol groups in mutual hydrogen bond interaction (OH_D acting as hydrogen bond donor and OH_A as hydrogen bond acceptor). The purpose of the ring was to impart some rigidity to the structure mimicking the real material. The intermolecular oxygen/oxygen distance controlling the strength of the mutual hydrogen bond was kept fixed at the specific distance, reported in the table of Fig. 2, while optimizing all other degrees of freedom, to simulate different situations present on the real silica surface. Vibrational frequencies in the harmonic approximation were evaluated on the final optimized structure. The adopted level of theory, which included the London dispersion interactions through the Grimme's empirical D3(BJ) correction (92) associated with the flexible 6-311++G(2d,2p) Gaussian basis set, minimized the basis set superposition error while describing charge polarization and electrostatics in an accurate way. The computer code used was from the Gaussian 09, Revision A.02 software (Gaussian). To calculate harmonic νOH values, the original DFT values were scaled by 0.959 (93). Harmonic νOD values were scaled with respect to νOH values using factors reported by Chakarova et al. (94).

The simulation of the phospholipid interacting with the NFS and isolated silanol silica models have been carried out by means of the recently developed new generic force field named GFN-FF, which enables fast structure optimizations and molecular-dynamics simulations for basically any chemical structure consisting of elements up to radon (95). GFN-FF is inspired by the latest developments in the field of semiempirical quantum methods, especially the GNF0-xTB (96) method. GFN-FF adopts the classical electronegativity-equilibrium atomic charge model (97, 98) for the description of pairwise interatomic electrostatic interactions. GFN-FF introduces approximations to the remaining quantum-mechanical terms in GFN0-xTB by replacing most of the extended-Hückel-type theory for covalent bonding by classical bond, angle, and torsion terms. The applications of GFN-FF to noncovalent interactions of the kind characterizing the present models showed excellent agreement for both structures and energetic with respect to density functional-based methods like B97-3c or even coupled cluster methods for water clusters at negligible computational cost.

Generation of Free Radicals in Acellular Systems. Free radical release was monitored by electron paramagnetic resonance (EPR) spectroscopy (Miniscope 100 EPR spectrometer; Magnettech) coupled with a spin trapping molecule (5,5-dimethylpirroline-*N*-oxide [DMPO]; Cayman Chemical Company). Hydroxyl radicals (HO˙) were detected by suspending silica samples (200 cm^2/mL) in PBS (10 mM, pH 7.4), DMPO (34 mM), and H_2O_2 (80 mM; Sigma-Aldrich). To represent the homolytic cleavage of C–H bonds in biomolecules, carboxylate radicals (COO^-) were assessed by suspending particles (2,000 cm^2/mL) in PBS (250 mM, pH 7.4), DMPO (85 mM), and sodium formate (1 M; Sigma-Aldrich). The instrument settings were as follows: microwave power, 10 mW; modulation, 1,000 mG; scan range, 120 G; and center of field, 3,345 G. Kinetics of radical release were monitored for 1 h. The experiments were repeated at least twice. The amount of radical released is proportional to the intensity of the EPR signal.

Membranolytic Activity. RBCs were purified from de-identified fresh human blood. Blood was collected in vacutainer tubes (S-monovette 8.2 mL 9NC; Sarstedt), and RBCs were purified by centrifugation at 300 × *g* for 10 min (Rotina 420R; Hettich) and washing four times with 0.9% NaCl (Baxter). RBCs were suspended in Dulbecco's PBS (DPBS) (Gibco) at the final concentration of 5% by volume. Silica samples were heated at 200 °C to inactivate any possible endotoxin or other microbial contaminants, then dispersed at the concentration of 300 cm^2/mL in DPBS and sonicated during 2 min in a bath (USC100T; VWR), just before testing. Serial dilutions of the starting dispersion were performed according to the final surface area doses used for experiments. Negative and positive controls consisted in DPBS and 0.1% Triton-X 100 (Sigma-Aldrich) in DPBS, respectively. Particle suspensions were incubated with RBCs on an orbital plate shaker at r.t. for 30 min, and then centrifuged at 300 × *g* for 10 min. Supernatants were transferred to a new plate, and the absorbance of the hemoglobin released was determined at 540 nm on a UV/vis spectrophotometer (Infinite F200; Tecan).

Cell Culture and Exposure to Particles. THP-1 cells (ATCC; TIB-202) were cultured at 37 °C and 5% CO_2 in complete medium, i.e., RPMI-1640 supplemented with 10% fetal bovine serum (FBS), 10 mM Hepes, and 1% antibiotic–antimycotic (Gibco). Cells were subcultured and exposed before reaching confluence. Before particle exposure, THP-1 cells were plated in 96-well plates (100,000 cells/well) in complete medium and differentiated from monocytes to macrophages with 100 nM phorbol 12-myristate 13-acetate (LC Laboratories) for 24 h. Next, cells were washed once with DPBS and exposed for 24 h to increasing concentrations of the particles previously heated at 200 °C for 2 h and then dispersed in culture medium without FBS. Supernatants of cell culture were collected and stored at −80 °C for cytokine assessment.

Quantification of IL-1β and Cell Viability Assessment. IL-1β was quantified by ELISA (limit of detection, 7.8 pg/mL; DY-201; DuoSet ELISA; R&D Systems) in cell culture supernatants following manufacturer's instructions. Cell viability was assessed on cells washed once with DPBS by the water-soluble tetrazolium salt (WST-1) assay (Roche), following manufacturer's instructions.

Animals and Particle Treatments. The protocol for rat experiments was approved by the local committee for animal research at the Université Catholique de Louvain, Comité d'Ethique pour l'Expérimentation Animale, Secteur des Sciences de la Santé, Brussels, Belgium (2018/UCL/MD/012). Eight-week-old female Wistar rats of ∼200 g were purchased from Janvier Labs. Animals were housed in positive pressure air-conditioned units (25 °C; 50% relative humidity) on a 12-h light/dark cycle, with ad libitum access to water and food. Rats were randomly allocated to experimental groups, and data collection and analysis were performed blind. Particles, previously heated at 200 °C for 2 h, were suspended in sterile 0.9% NaCl. After anesthesia with 200 μL of Nimatek (i.p.; 37.5 mg/mL; Eurovet) and Rompun (0.5%; Bayer), 300 μL of particle suspensions or 0.9% NaCl (Ctl) were administered by oropharyngeal aspiration (o.p.a.). This procedure is a convenient alternative to inhalation exposure for initial hazard identification and induces qualitatively similar lung responses as after inhalation exposure (99). A dose of 0.75 mg of particles was selected to avoid lung particle overload (100). Higher doses were also used for gQ and gQ-f (2.5 and 5 mg) to appreciate differences between the paired samples (*SI Appendix*, Fig. S4 *C–F*). Animals were killed 3 d after particle administration with an overdose of sodium pentobarbital (30 mg/rat, i.p.; Certa S.A.).

Bronchoalveolar Lavage and Inflammatory Markers Assessment. Bronchoalveolar lavage (BAL) was performed by cannulating the trachea and infusing the lungs with 6 mL of 0.9% NaCl. BAL fluid (BALF) was centrifuged 10 min at 240 × *g* and 4 °C. Cell-free supernatant of BALF was used for biochemical measurements. The cell pellet was resuspended in 0.9% NaCl, and total BAL cells were counted with Turk's solution (1% crystal violet and 3% acetic acid). Remaining cells were cytocentrifuged on slides, stained with Diff-Quick (Polysciences), imaged with a Leica SCN400 slide scanner, and analyzed with the Leica Aperio ImageScope software. Lactate dehydrogenase (LDH) activity, total protein content, and myeloperoxidase (MPO) activity were assayed on BALF as described previously (101). MPO is a suitable marker of neutrophilic infiltration, as is predominantly expressed in neutrophils, and of pulmonary toxicity of inorganic particles (102). LDH activity reflects cytotoxicity mainly to macrophages, and total proteins are related to both increased alveolocapillary permeability and local inflammatory reaction (103).

Mutagenicity. The mutagenic response was evaluated through an ex vivo micronucleus assay on type II alveolar epithelial cells, adapting a protocol used in previous studies (104), as described in detail in *SI Appendix*. Eight-week-old female Wistar rats (Janvier Labs) were treated by o.p.a. with an inflammatory dose (0.75 mg) of quartz particles or the positive reference particle WC-Co (2 mg) (89). Briefly, after 3 d, rats were killed, and type II alveolar epithelial cells were collected from lavaged and digested lungs. Fc receptor-negative cells were incubated 2 d at 37 °C and 5% CO_2, stained with acridine orange, and analyzed for micronuclei with a fluorescence microscope.

Statistics. Statistical parameters, including the number of independent experiments, the number of biological replicates per experiment, and statistical significance, are reported in the figures and figure legends. Normally distributed data were analyzed by two-tailed unpaired Student's *t* test, one-way or two-way ANOVA followed by Dunnett's post hoc test, as appropriate. In all tests, a 95% confidence interval was used, for which differences with $P < 0.05$ were considered statistically significant. Unless otherwise stated, data

are presented as mean ± SEM. Statistical analysis was performed with the GraphPad Prism 8 software (GraphPad Software).

Data and Code Availability. All of the study data are included in the manuscript and *SI Appendix*.

ACKNOWLEDGMENTS. The study was supported by the European Association of Industrial Silica Producers. We thank Violaine Sironval (Louvain Centre for Toxicology and Applied Pharmacology, Université Catholique de Louvain) for assisting with in vivo protocols, and Linda Pastero (Department of Earth Sciences, University of Turin) for support with quartz synthesis and characterization. Some toxicological measurements were carried out with equipment of the imaging platform of the Institute of Experimental and Clinical Research (UCLouvain). While waiting for this article to be published, Prof. Gianmario Martra suddenly left us. Gianmario was an outstanding researcher, teacher, and mentor, who never stopped learning while tirelessly supporting young people in their scientific trajectory. During his remarkable academic career, he developed vast and yet amazingly deep scientific interests. Beside his scientific achievement, he was loved by all students for his continuous encouragement and dedication helping everybody to feel the mystery and beauty of discovery in science. We are dedicating this research to his memory.

1. L. Addadi, N. Rubin, L. Scheffer, R. Ziblat, Two and three-dimensional pattern recognition of organized surfaces by specific antibodies. *Acc. Chem. Res.* **41**, 254–264 (2008).
2. D. Hanein, B. Geiger, L. Addadi, Differential adhesion of cells to enantiomorphous crystal surfaces. *Science* **263**, 1413–1416 (1994).
3. Y. Y. Hu, A. Rawal, K. Schmidt-Rohr, Strongly bound citrate stabilizes the apatite nanocrystals in bone. *Proc. Natl. Acad. Sci. U.S.A.* **107**, 22425–22429 (2010).
4. P. Thevenot, W. Hu, L. Tang, Surface chemistry influences implant biocompatibility. *Curr. Top. Med. Chem.* **8**, 270–280 (2008).
5. M. F. Bachmann, G. T. Jennings, Vaccine delivery: A matter of size, geometry, kinetics and molecular patterns. *Nat. Rev. Immunol.* **10**, 787–796 (2010).
6. M. Lundqvist *et al*., Nanoparticle size and surface properties determine the protein corona with possible implications for biological impacts. *Proc. Natl. Acad. Sci. U.S.A.* **105**, 14265–14270 (2008).
7. A. E. Nel *et al*., Understanding biophysicochemical interactions at the nano-bio interface. *Nat. Mater.* **8**, 543–557 (2009).
8. B. Fubini, Surface reactivity in the pathogenic response to particulates. *Environ. Health Perspect.* **105** (suppl. 5), 1013–1020 (1997).
9. R. K. Iler, *The Chemistry of Silica: Solubility, Polymerization, Colloid and Surface Properties, and Biochemistry* (Wiley, 1979), pp. 3–10, 624–648.
10. A. Rimola, D. Costa, M. Sodupe, J. F. Lambert, P. Ugliengo, Silica surface features and their role in the adsorption of biomolecules: Computational modeling and experiments. *Chem. Rev.* **113**, 4216–4313 (2013).
11. A. K. Mishra, R. Belgamwar, R. Jana, A. Datta, V. Polshettiwar, Defects in nanosilica catalytically convert CO_2 to methane without any metal and ligand. *Proc. Natl. Acad. Sci. U.S.A.* **117**, 6383–6390 (2020).
12. J. Shi, P. W. Kantoff, R. Wooster, O. C. Farokhzad, Cancer nanomedicine: Progress, challenges and opportunities. *Nat. Rev. Cancer* **17**, 20–37 (2017).
13. A. Rimola, M. Fabbiani, M. Sodupe, P. Ugliengo, G. Martra, How does silica catalyze the amide bond formation under dry conditions? Role of specific surface silanol pairs. *ACS Catal.* **8**, 4558–4568 (2018).
14. P. Cullinan *et al*., Occupational lung diseases: From old and novel exposures to effective preventive strategies. *Lancet Respir. Med.* **5**, 445–455 (2017).
15. R. F. Hoy, D. C. Chambers, Silica-related diseases in the modern world. *Allergy* **00**, 1–13 (2020).
16. C. C. Leung, I. T. S. Yu, W. Chen, Silicosis. *Lancet* **379**, 2008–2018 (2012).
17. K. M. Pollard, Silica, silicosis, and autoimmunity. *Front. Immunol.* **7**, 97 (2016).
18. GBD 2017 Causes of Death Collaborators, Global, regional, and national age-sex-specific mortality for 282 causes of death in 195 countries and territories, 1980–2017: A systematic analysis for the Global Burden of Disease Study 2017. *Lancet* **392**, 1736–1788 (2018).
19. International Agency for Research on Cancer (IARC), "Silica", in *Silica, some silicates, coal dust and para-aramid fibrils. IARC Monogr. Eval. Carcinog. Risks Hum.* **68**, 39–242 (1997).
20. International Agency for Research on Cancer (IARC), "Silica dust, crystalline, in the form of quartz or cristobalite" in *Arsenic, Metals, Fibres, and Dusts, IARC Monogr. Eval. Carcinog. Risks Hum. 100C*, (International Agency for Research on Cancer, 2012), pp. 355–406.
21. V. Hornung *et al*., Silica crystals and aluminum salts activate the NALP3 inflammasome through phagosomal destabilization. *Nat. Immunol.* **9**, 847–856 (2008).
22. C. Dostert *et al*., Innate immune activation through Nalp3 inflammasome sensing of asbestos and silica. *Science* **320**, 674–677 (2008).
23. S. L. Cassel *et al*., The Nalp3 inflammasome is essential for the development of silicosis. *Proc. Natl. Acad. Sci. U.S.A.* **105**, 9035–9040 (2008).
24. T. Skuland *et al*., Pro-inflammatory effects of crystalline- and nano-sized non-crystalline silica particles in a 3D alveolar model. *Part. Fibre Toxicol.* **17**, 13 (2020).
25. S. Murugadoss *et al*., Toxicology of silica nanoparticles: An update. *Arch. Toxicol.* **91**, 2967–3010 (2017).
26. D. Napierska, L. C. J. Thomassen, D. Lison, J. A. Martens, P. H. Hoet, The nanosilica hazard: Another variable entity. *Part. Fibre Toxicol.* **7**, 39 (2010).
27. B. T. Mossman, A. Churg, Mechanisms in the pathogenesis of asbestosis and silicosis. *Am. J. Respir. Crit. Care Med.* **157**, 1666–1680 (1998).
28. R. Merget *et al*., Health hazards due to the inhalation of amorphous silica. *Arch. Toxicol.* **75**, 625–634 (2002).
29. C. Pavan, B. Fubini, Unveiling the variability of "quartz hazard" in light of recent toxicological findings. *Chem. Res. Toxicol.* **30**, 469–485 (2017).
30. H. Zhang *et al*., Processing pathway dependence of amorphous silica nanoparticle toxicity: Colloidal vs pyrolytic. *J. Am. Chem. Soc.* **134**, 15790–15804 (2012).
31. L. Rubio *et al*., Safer-by-design flame-sprayed silicon dioxide nanoparticles: The role of silanol content on ROS generation, surface activity and cytotoxicity. *Part. Fibre Toxicol.* **16**, 40 (2019).
32. A. D. Maynard, Old materials, new challenges? *Nat. Nanotechnol.* **9**, 658–659 (2014).
33. G. Cerrato, B. Fubini, M. Baricco, C. Morterra, Spectroscopic, structural and microcalorimetric study of stishovite, a nonpathogenic polymorph of SiO_2. *J. Mater. Chem.* **5**, 1935–1941 (1995).
34. F. Turci *et al*., Revisiting the paradigm of silica pathogenicity with synthetic quartz crystals: The role of crystallinity and surface disorder. *Part. Fibre Toxicol.* **13**, 32 (2016).
35. B. Sun *et al*., Repetitive dosing of fumed silica leads to profibrogenic effects through unique structure-activity relationships and biopersistence in the lung. *ACS Nano* **10**, 8054–8066 (2016).
36. A. S. Morris *et al*., Amine modification of nonporous silica nanoparticles reduces inflammatory response following intratracheal instillation in murine lungs. *Toxicol. Lett.* **241**, 207–215 (2016).
37. M. Yang *et al*., Macrophages participate in local and systemic inflammation induced by amorphous silica nanoparticles through intratracheal instillation. *Int. J. Nanomedicine* **11**, 6217–6228 (2016).
38. C. Pavan *et al*., The puzzling issue of silica toxicity: Are silanols bridging the gaps between surface states and pathogenicity? *Part. Fibre Toxicol.* **16**, 32 (2019).
39. P. B. Dempster, P. D. Ritchie, G. Nagel-Schmidt, R. L. Gordon, O. G. Griffin, Surface of finely-ground silica. *Nature* **169**, 539–540 (1952).
40. A. M. Schrader *et al*., Surface chemical heterogeneity modulates silica surface hydration. *Proc. Natl. Acad. Sci. U.S.A.* **115**, 2890–2895 (2018).
41. A. Burneau, J.-P. Gallas, "Hydroxyl groups on silica surfaces" in *The Surface Properties of Silicas*, A. P. Legrand, Ed. (Wiley, 1998), pp. 145–312.
42. T. Nash, A. C. Allison, J. S. Harington, Physico-chemical properties of silica in relation to its toxicity. *Nature* **210**, 259–261 (1966).
43. R. P. Nolan, A. M. Langer, J. S. Harington, G. Oster, I. J. Selikoff, Quartz hemolysis as related to its surface functionalities. *Environ. Res.* **26**, 503–520 (1981).
44. C. Pavan, V. Rabolli, M. Tomatis, B. Fubini, D. Lison, Why does the hemolytic activity of silica predict its pro-inflammatory activity? *Part. Fibre Toxicol.* **11**, 76 (2014).
45. C. Pavan *et al*., In search of the chemical basis of the hemolytic potential of silicas. *Chem. Res. Toxicol.* **26**, 1188–1198 (2013).
46. L. Pastero, F. Turci, R. Leinardi, C. Pavan, M. Monopoli, Synthesis of α-quartz with controlled properties for the investigation of the molecular determinants in silica toxicology. *Cryst. Growth Des.* **16**, 2394–2403 (2016).
47. S. Lu *et al*., Efficacy of simple short-term in vitro assays for predicting the potential of metal oxide nanoparticles to cause pulmonary inflammation. *Environ. Health Perspect.* **117**, 241–247 (2009).
48. F. Musso, S. Casassa, M. Corno, P. Ugliengo, How strong are H-bonds at the fully hydroxylated silica surfaces? Insights from the B3LYP electron density topological analysis. *Struct. Chem.* **28**, 1009–1015 (2017).
49. C. Carteret, Mid- and near-infrared study of hydroxyl groups at a silica surface: H-bond effect. *J. Phys. Chem. C* **113**, 13300–13308 (2009).
50. F. Catalano, G. Alberto, P. Ivanchenko, G. Dovbeshko, G. Martra, Effect of silica surface properties on the formation of multilayer or submonolayer protein hard corona: Albumin adsorption on pyrolytic and colloidal SiO_2 nanoparticles. *J. Phys. Chem. C* **119**, 26493–26505 (2015).
51. R. S. Pandurangi, M. S. Seehra, B. L. Razzaboni, P. Bolsaitis, Surface and bulk infrared modes of crystalline and amorphous silica particles: A study of the relation of surface structure to cytotoxicity of respirable silica. *Environ. Health Perspect.* **86**, 327–336 (1990).
52. B. Fubini *et al*., Relationship between surface properties and cellular responses to crystalline silica: Studies with heat-treated cristobalite. *Chem. Res. Toxicol.* **12**, 737–745 (1999).
53. B. Sun *et al*., Reduction of acute inflammatory effects of fumed silica nanoparticles in the lung by adjusting silanol display through calcination and metal doping. *ACS Nano* **9**, 9357–9372 (2015).
54. F. Musso, P. Ugliengo, M. Sodupe, Do H-bond features of silica surfaces affect the H_2O and NH_3 adsorption? Insights from periodic B3LYP calculations. *J. Phys. Chem. A* **115**, 11221–11228 (2011).
55. P. J. A. Borm, P. Fowler, D. Kirkland, An updated review of the genotoxicity of respirable crystalline silica. *Part. Fibre Toxicol.* **15**, 23 (2018).
56. A. Lesniak *et al*., Effects of the presence or absence of a protein corona on silica nanoparticle uptake and impact on cells. *ACS Nano* **6**, 5845–5857 (2012).
57. S. V. Patwardhan *et al*., Chemistry of aqueous silica nanoparticle surfaces and the mechanism of selective peptide adsorption. *J. Am. Chem. Soc.* **134**, 6244–6256 (2012).

58. K. Leung, I. M. Nielsen, L. J. Criscenti, Elucidating the bimodal acid-base behavior of the water-silica interface from first principles. *J. Am. Chem. Soc.* **131**, 18358–18365 (2009).
59. M. S. Azam, C. N. Weeraman, J. M. Gibbs-Davis, Specific cation effects on the bimodal acid-base behavior of the silica/water interface. *J. Phys. Chem. Lett.* **3**, 1269–1274 (2012).
60. F. Musso, M. Sodupe, M. Corno, P. Ugliengo, H-bond features of fully hydroxylated surfaces of crystalline silica polymorphs: A periodic B3LYP study. *J. Phys. Chem. C* **113**, 17876–17884 (2009).
61. F. Musso, P. Mignon, P. Ugliengo, M. Sodupe, Cooperative effects at water-crystalline silica interfaces strengthen surface silanol hydrogen bonding. An ab initio molecular dynamics study. *Phys. Chem. Chem. Phys.* **14**, 10507–10514 (2012).
62. J. H. Wiessner, J. D. Henderson, Jr, P. G. Sohnle, N. S. Mandel, G. S. Mandel, The effect of crystal structure on mouse lung inflammation and fibrosis. *Am. Rev. Respir. Dis.* **138**, 445–450 (1988).
63. L. Di Cristo *et al*., Pro-inflammatory effects of pyrogenic and precipitated amorphous silica nanoparticles in innate immunity cells. *Toxicol. Sci.* **150**, 40–53 (2016).
64. B. Fubini, A. Hubbard, Reactive oxygen species (ROS) and reactive nitrogen species (RNS) generation by silica in inflammation and fibrosis. *Free Radic. Biol. Med.* **34**, 1507–1516 (2003).
65. X. Shi *et al*., Reactive oxygen species and molecular mechanism of silica-induced lung injury. *J. Environ. Pathol. Toxicol. Oncol.* **20** (suppl. 1), 85–93 (2001).
66. R. F. Hamilton, Jr, S. A. Thakur, A. Holian, Silica binding and toxicity in alveolar macrophages. *Free Radic. Biol. Med.* **44**, 1246–1258 (2008).
67. J. Øvrevik, M. Refsnes, M. Låg, J. A. Holme, P. E. Schwarze, Activation of proinflammatory responses in cells of the airway mucosa by particulate matter: Oxidant- and non-oxidant-mediated triggering mechanisms. *Biomolecules* **5**, 1399–1440 (2015).
68. M. Wang *et al*., Silica nanoparticles induce lung inflammation in mice via ROS/PARP/TRPM2 signaling-mediated lysosome impairment and autophagy dysfunction. *Part. Fibre Toxicol.* **17**, 23 (2020).
69. M. Pozzolini *et al*., Different reactivity of primary fibroblasts and endothelial cells towards crystalline silica: A surface radical matter. *Toxicology* **361-362**, 12–23 (2016).
70. A. Clouter, D. Brown, D. Höhr, P. Borm, K. Donaldson, Inflammatory effects of respirable quartz collected in workplaces versus standard DQ12 quartz: Particle surface correlates. *Toxicol. Sci.* **63**, 90–98 (2001).
71. V. Vallyathan, Generation of oxygen radicals by minerals and its correlation to cytotoxicity. *Environ. Health Perspect.* **102** (suppl. 10), 111–115 (1994).
72. N. S. Dalal, X. L. Shi, V. Vallyathan, Role of free radicals in the mechanisms of hemolysis and lipid peroxidation by silica: Comparative ESR and cytotoxicity studies. *J. Toxicol. Environ. Health* **29**, 307–316 (1990).
73. C. Leonard *et al*., Contribution of plasma membrane lipid domains to red blood cell (re)shaping. *Sci. Rep.* **7**, 4264 (2017).
74. A. C. Dumitru *et al*., Nanoscale membrane architecture of healthy and pathological red blood cells. *Nanoscale Horiz.* **3**, 293–304 (2018).
75. K. Simons, J. Gruenberg, Jamming the endosomal system: Lipid rafts and lysosomal storage diseases. *Trends Cell Biol.* **10**, 459–462 (2000).
76. G. van Meer, D. R. Voelker, G. W. Feigenson, Membrane lipids: Where they are and how they behave. *Nat. Rev. Mol. Cell Biol.* **9**, 112–124 (2008).
77. D. K. Murray, J. C. Harrison, W. E. Wallace, A ^{13}C CP/MAS and ^{31}P NMR study of the interactions of dipalmitoylphosphatidylcholine with respirable silica and kaolin. *J. Colloid Interface Sci.* **288**, 166–170 (2005).
78. Y. Chunbo, Z. Daqing, L. Aizhuo, N. Jiazuan, A NMR study of the interaction of silica with dipalmitoylphosphatidylcholine liposomes. *J. Colloid Interface Sci.* **172**, 536–538 (1995).
79. R. Leinardi *et al*., Cytotoxicity of fractured quartz on THP-1 human macrophages: Role of the membranolytic activity of quartz and phagolysosome destabilization. *Arch. Toxicol.* **94**, 2981–2995 (2020).
80. V. Rabolli, D. Lison, F. Huaux, The complex cascade of cellular events governing inflammasome activation and IL-1β processing in response to inhaled particles. *Part. Fibre Toxicol.* **13**, 40 (2016).
81. T. Morishige *et al*., The effect of surface modification of amorphous silica particles on NLRP3 inflammasome mediated IL-1beta production, ROS production and endosomal rupture. *Biomaterials* **31**, 6833–6842 (2010).
82. W. J. Sandberg *et al*., Comparison of non-crystalline silica nanoparticles in IL-1β release from macrophages. *Part. Fibre Toxicol.* **9**, 32 (2012).
83. M. Winter *et al*., Activation of the inflammasome by amorphous silica and TiO_2 nanoparticles in murine dendritic cells. *Nanotoxicology* **5**, 326–340 (2011).
84. F. Martinon, V. Pétrilli, A. Mayor, A. Tardivel, J. Tschopp, Gout-associated uric acid crystals activate the NALP3 inflammasome. *Nature* **440**, 237–241 (2006).
85. C. J. Johnston *et al*., Pulmonary chemokine and mutagenic responses in rats after subchronic inhalation of amorphous and crystalline silica. *Toxicol. Sci.* **56**, 405–413 (2000).
86. F. Roelofs, W. Vogelsberger, Dissolution kinetics of synthetic amorphous silica in biological-like media and its theoretical description. *J. Phys. Chem. B* **108**, 11308–11316 (2004).
87. J. H. Arts, H. Muijser, E. Duistermaat, K. Junker, C. F. Kuper, Five-day inhalation toxicity study of three types of synthetic amorphous silicas in Wistar rats and post-exposure evaluations for up to 3 months. *Food Chem. Toxicol.* **45**, 1856–1867 (2007).
88. M. Ghiazza *et al*., Does vitreous silica contradict the toxicity of the crystalline silica paradigm? *Chem. Res. Toxicol.* **23**, 620–629 (2010).
89. M. De Boeck *et al*., In vivo genotoxicity of hard metal dust: Induction of micronuclei in rat type II epithelial lung cells. *Carcinogenesis* **24**, 1793–1800 (2003).
90. G. Lasfargues, D. Lison, P. Maldague, R. Lauwerys, Comparative study of the acute lung toxicity of pure cobalt powder and cobalt-tungsten carbide mixture in rat. *Toxicol. Appl. Pharmacol.* **112**, 41–50 (1992).
91. A. D. Becke, Density-functional thermochemistry. III. The role of exact exchange. *J. Chem. Phys.* **98**, 5648–5652 (1993).
92. S. Grimme, S. Ehrlich, L. Goerigk, Effect of the damping function in dispersion corrected density functional theory. *J. Comput. Chem.* **32**, 1456–1465 (2011).
93. S. Tosoni *et al*., Quantum mechanical calculation of the OH vibrational frequency in crystalline solids. *Mol. Phys.* **103**, 2549–2558 (2005).
94. K. Chakarova, N. Drenchev, M. Mihaylov, P. Nikolov, K. Hadjiivanov, OH/OD isotopic shift factors of isolated and H-bonded surface silanol groups. *J. Phys. Chem. C* **117**, 5242–5248 (2013).
95. S. Spicher, S. Grimme, Robust atomistic modeling of materials, organometallic, and biochemical systems. *Angew. Chem. Int. Ed. Engl.* **132**, 2–11 (2020).
96. P. Pracht, E. Caldeweyher, S. Ehlert, S. Grimme, A robust non-self-consistent tight-binding quantum chemistry method for large molecules. 10.26434/chemrxiv.8326202.v1 (27 June 2019).
97. W. J. Mortier, S. K. Ghosh, S. Shankar, Electronegativity-equalization method for the calculation of atomic charges in molecules. *J. Am. Chem. Soc.* **108**, 4315–4320 (1986).
98. S. A. Ghasemi, A. Hofstetter, S. Saha, S. Goedecker, Interatomic potentials for ionic systems with density functional accuracy based on charge densities obtained by a neural network. *Phys. Rev. B Condens. Matter Mater. Phys.* **92**, 045131 (2015).
99. P. Kinaret *et al*., Inhalation and oropharyngeal aspiration exposure to rod-like carbon nanotubes induce similar airway inflammation and biological responses in mouse lungs. *ACS Nano* **11**, 291–303 (2017).
100. P. Borm, F. R. Cassee, G. Oberdörster, Lung particle overload: Old school—new insights? *Part. Fibre Toxicol.* **12**, 10 (2015).
101. V. Rabolli *et al*., Lung fibrosis induced by crystalline silica particles is uncoupled from lung inflammation in NMRI mice. *Toxicol. Lett.* **203**, 127–134 (2011).
102. T. Tomonaga *et al*., Usefulness of myeloperoxidase as a biomarker for the ranking of pulmonary toxicity of nanomaterials. *Part. Fibre Toxicol.* **15**, 41 (2018).
103. R. F. Henderson *et al*., New approaches for the evaluation of pulmonary toxicity: Bronchoalveolar lavage fluid analysis. *Fundam. Appl. Toxicol.* **5**, 451–458 (1985).
104. J. Muller *et al*., Clastogenic and aneugenic effects of multi-wall carbon nanotubes in epithelial cells. *Carcinogenesis* **29**, 427–433 (2008).